EDGE ARTICLE

Check for updates

Achieving high efficiency ultrapure violet OLEDs with a CIE$_y$ coordinate of below 0.015 through precise manipulation of peripheral heavy atom sulfur

Rui Chen, [ID] [a] Shengyu Li,[a] Hao Huang,[a] Xingwen Tong,[b] Yuchao Liu, [ID] [a] Zhongjie Ren, [ID] [b] Shian Ying, [ID] *[a] Liqun Liu*[c] and Shouke Yan [ID] *[ab]

The development of efficient pure violet organic light-emitting diodes (OLEDs) featuring a low Commission Internationale de l'Éclairage (CIE)$_y$ coordinate of below 0.02 remains a critical yet challenging objective. Herein, three ultrapure violet hot-exciton emitters, namely BO-2DBT, BO-3DBT, and BO-4DBT, have been developed through strategic integration of an oxygen-bridged cyclized boron (BO) skeleton with a dibenzothiophene (DBT) at varied substitution positions, where the effect of the regioisomerism of heavy sulfur atom was investigated. All three emitters demonstrate narrowband violet emission in toluene solution, with maxima centered at 405, 408, and 404 nm, respectively, and narrow full widths at half-maximum (FWHM) of 23, 22, and 22 nm, respectively. Theoretical analyses reveal significant high-lying reverse intersystem crossing rates (10^6–10^7 s^{-1}) across all emitters. Notably, BO-2DBT exhibits superior fluorescence efficiency, with its intersystem crossing rate from S$_1$ to T$_1$ reduced by over one order of magnitude compared to others, attributable to minimal spin−orbit coupling (0.059 cm^{-1}). Consequently, the optimized device employing BO-2DBT as an emitter achieves ultrapure violet electroluminescence with a peak at 405 nm, FWHM of 25 nm, and CIE coordinates of (0.166, 0.014). The device demonstrates a peak external quantum efficiency of 7.90%, retaining 7.67% at 500 cd m^{-2}. To the best of our knowledge, this work represents the first report of ultrapure violet OLEDs with a CIE$_y$ coordinate <0.015 and establishes a new efficiency benchmark for this class of devices.

Introduction

With the rapid progress of organic light-emitting diode (OLED) technology in the realm of wide-color-gamut high-definition and ultra-high-definition displays, red, green, and blue (RGB) emitting materials with high color purity have emerged as the focal point of extensive research attention. Numerous monochromatic RGB OLEDs, featuring external quantum efficiencies (EQEs) exceeding 20% and narrow emission spectra with a full width at half-maximum (FWHM) of less than 30 nm, have been developed. In contrast, despite the significant application value

of violet materials in various fields such as photodynamic therapy, high-density information storage, anti-counterfeiting, non-antibiotic treatment, photocuring, and other sensing and medical applications,[1–5] highly efficient violet OLEDs, especially narrowband violet OLEDs with a Commission Internationale de l'Éclairage (CIE)$_y$ value of below 0.02,[6,7] have been rarely reported.

Most violet OLEDs suffer from limited color purity due to their broad emission spectra which originate from the structural relaxation and intrinsic vibrational coupling occurring between the lowest excited singlet state (S$_1$) and the ground state (S$_0$).[8,9] To improve the color purity with a small FWHM value, a traditionally common approach is to introduce color filters or optical microcavity techniques to cut off the edge regions of the electroluminescence (EL) spectrum within the device, leading to a significant energy loss.[8,10] In 2016, Hatakeyama *et al.* pioneered a unique molecular design concept of multiple resonance (MR) effect induced narrowband emitter, in which the electron-rich heteroatom (N/O) and electron-deficient boron (B) were embedded in polycyclic aromatic hydrocarbons. The rigid molecular structure can effectively suppress vibronic coupling and structural alterations in the excited state,

[a]State Key Laboratory of Advanced Optical Polymer and Manufacturing Technology, Key Laboratory of Rubber-Plastics, Ministry of Education, Qingdao University of Science and Technology, Qingdao 266042, P. R. China. E-mail: shian0610@126.com; skyan@mail.buct.edu.cn

[b]State Key Laboratory of Chemical Resource Engineering, College of Materials Science and Engineering, Beijing University of Chemical Technology, Beijing 100029, P. R. China

[c]State Key Laboratory of Luminescent Materials and Devices, Institute of Polymer Optoelectronic Materials and Devices, Guangdong Basic Research Center of Excellence for Energy and Information Polymer Materials, South China University of Technology, Guangzhou 510640, P. R. China. E-mail: liqun.liu@foxmail.com

resulting in an unprecedented color purity with a small FWHM.[11–13] Moreover, the unique short-range charge transfer (SR-CT) state induced by the atomical separation of frontier molecular orbitals (FMOs) endows MR-emitters with a high radiative transition rate (k_r).[14] Based on the oxygen-bridged cyclized boron (BO) type MR skeleton, Zhao *et al.* reported an intramolecular through-space charge transfer (TSCT) molecule *t*Cz-BO-PCz, providing narrow ultraviolet light with an EL peak at 398 nm, a FWHM value of 32 nm, a CIE_y value of 0.023, and an EQE of 3.82%;[15] Lee and colleagues reported a pure violet emitter BO-2mSi, demonstrating an EQE of 7.1%, a FWHM of 33 nm, and color coordinates of (0.16, 0.02);[16] Zhu *et al.* achieved a high EQE of 9.15%, an EL peak at 414 nm, a FWHM of 32 nm, and color coordinates of (0.165, 0.034) in a solution-processed OLED with tBOSi as a dopant.[17] Recently, Zhu *et al.* reported an efficient hybridized local and charge transfer (HLCT) molecule ICz-BO, achieving a recorded maximum EQE of 12.01%, as well as pure violet emission with an EL peak at 414 nm, a FWHM of 32 nm, and CIE coordinates of (0.164, 0.031).[13] However, as the drive current increases for higher light output, EQEs steeply decline (known as efficiency roll-off), due to the serious exciton quenching processes associated with a critical triplet-to-singlet spin-flipping process.

In accordance with first-order perturbation theory, the spin–orbital coupling (SOC) matrix element between the initial triplet and final singlet states emerges as a pivotal factor influencing the spin-flipping dynamics.[18,19] The judicious integration of heavy atoms within organic emitters has been successfully harnessed to engineer thermally activated delayed fluorescent (TADF) and phosphorescent materials that exhibit pronounced SOC effects.[20,21] Such integration facilitates rapid intersystem crossing and reverse intersystem crossing (ISC and RISC) processes, ultimately mitigating the notorious efficiency roll-off phenomenon to a considerable degree. Meanwhile, it has been often observed that heavy atoms in the MR skeleton, due to their large atomic radius, induce greater conformational flexibility, thus resulting in the unexpected spectrum broadening issue. Furthermore, until now, no research has elucidated the influence of precise positional modulation of heavy atoms within the molecular structure of ultraviolet emitters on their optoelectronic properties.

In this study, we present a feasible strategy for designing highly efficient donor–acceptor (D–A) type pure violet emitters by meticulously modulating the peripheral substitution site of heterocyclic donor, dibenzothiophene (DBT) containing the moderately heavy sulfur atom, on the prototypical MR-type electron acceptor. Here, 5,9-dioxa-13b-boranaphtho[3,2,1-*de*]anthracene (DOBNA), featuring a prominent emission band centered at 398 nm,[22] serves as an MR-type acceptor, where two *tert*-butyl group are introduced to lower the lowest unoccupied molecular orbital (LUMO) energy level,[23] as well as to enhance the solubility and quenching resistance caused by intermolecular interactions. Consequently, three emitters: BO-2DBT, BO-3DBT, and BO-4DBT are synthesized with 2-, 3-, and 4-substituted DBT, respectively (Fig. 1). All the emitters exhibit similar electronic transitions in the lowest singlet (S$_1$) state, retaining ultrapure violet emission with the peak wavelengths
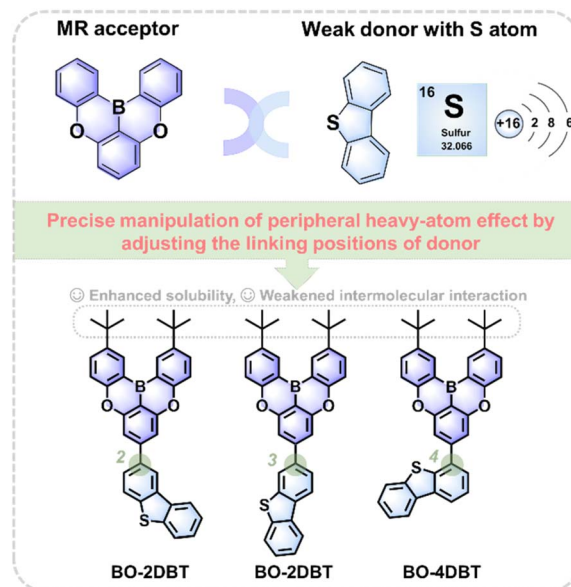

Fig. 1 Schematic illustration of pure violet emitter design strategy by combining DBT with an MR-type acceptor.

of 404–408 nm and narrow FWHMs of 22–23 nm in toluene solution. For BO-4DBT with 4-substituted DBT, the greatest change in electronic configuration between the S$_1$ and its energetically close fifth triplet (T$_5$) state leads to a significantly large SOC matrix element of 0.857 cm^{-1}, resulting in a fast reverse intersystem crossing rate (k_{RISC}). Whereas, its photoluminescence quantum yields (PLQYs) decrease obviously due to the slow radiative transition process. Owing to the better trade-off between them, BO-2DBT exhibits enhanced EL performance. The optimized OLED based on BO-2DBT not only displays narrowband violet emission peaking at 405 nm with a FWHM value of 25 nm, corresponding to CIE coordinates of (0.166, 0.014), but also achieves an impressive EQE$_{max}$ of 7.90%, representing the state-of-the-art EL performance in violet OLEDs with a CIE_y value below 0.02.

Results and discussion

Molecular synthesis and characterization

The synthetic routes of target materials BO-2DBT, BO-3DBT, and BO-4DBT are shown in Scheme S1. All the compounds were synthesized by a typical palladium-catalyzed Suzuki cross-coupling reaction (Scheme S1, SI) between DBT boric acid molecules and 7-bromo-2,12-di-*tert*-butyl-5,9-dioxa-13b-boranaphtho[3,2,1-*de*]anthracene (BO-Br), while BO-Br was obtained by a two-step reaction.[24] After purification by column chromatography and vacuum sublimation, the molecular structures of BO-2DBT, BO-3DBT, and BO-4DBT were characterized using ^{1}H and ^{13}C nuclear magnetic resonance (NMR) and high-resolution mass spectra (HRMS) (Fig. S1–S13, SI). Thermogravimetric analysis (TGA) reveals that all the compounds have excellent thermal stabilities with decomposition temperatures (T_d, at 5% weight loss) of 387, 415 and 364 °C for BO-2DBT, BO-3DBT, and BO-4DBT, respectively (Fig. S14).

The glass transition temperature (T_g) of BO-4DBT is 162 °C, while no significant T_g is observed for BO-2DBT and BO-3DBT (Fig. S15). The electrochemical properties of the three molecules were investigated by cyclic voltammetry (CV) in degassed acetonitrile (Fig. S16). The highest occupied molecular orbital (HOMO) energies for BO-2DBT, BO-3DBT, and BO-4DBT are −5.75, −5.78 and −5.86 eV, respectively. The LUMO energies of BO-2DBT, BO-3DBT, and BO-4DBT are calculated to be −2.66, −2.72 and −2.76 eV, respectively, according to the difference between the HOMO and the optical bandgap (E_g).

Theoretical calculation

To elucidate the relationship between the molecular structure modifications and electronic properties for the three emitters, density functional theory (DFT) and time-dependent DFT (TD-DFT) calculations were further performed at the PBE0/6-31G (d, p) level.[25,26] As shown in Fig. 2, these compounds display moderately distorted and rigid S_0 geometries with torsion angles of 37.7°, 37.5° and 47.9° between the BO acceptor and DBT donor, respectively, whereas the torsion angles decrease to 31.8°, 26.3° and 40.0°, respectively, in the optimized S_1 geometries. This planarization feature is conducive to enhancing radiative transitions while limiting the molecular conjugation length, thereby enabling the construction of wide bandgap emitters with high fluorescence efficiency.[27,28] Meanwhile, BO-2DBT, BO-3DBT, and BO-4DBT demonstrate small root-mean-square displacement (RMSD) values of 0.214–0.224 Å, as well as small total reorganization energies of 0.188–0.199 eV between the S_0 and S_1 states (Fig. 2 and S17), indicating the suppressed geometrical deformation in the excitation–emission processes, aligning well with the observed small Stokes shift and small FWHM in the experiment.[29] The HOMOs of all the emitters are uniformly located on the BO unit, while their LUMOs are mainly localized on the BO unit and extend to the DBT moiety. As shown by the natural transition orbital (NTO) analysis in Fig. 3, the S_1 states of BO-2DBT, BO-3DBT, and BO-4DBT show two possible transition components with a degree of orbital overlaps indicated by the overlap integrals (62.47% for BO-2DBT, 61.67% for BO-3DBT, and 62.94% for BO-4DBT) between the hole and electron distributions, including the SR-CT transition originating from the MR effect of the boron and oxygen atoms within the BO unit and long-range charge transfer (LR-CT) transition between the BO unit and the peripheral DBT unit, which possess substantial potential for achieving narrowband emission.[30] The oscillator strengths for BO-2DBT, BO-3DBT, and BO-4DBT, are as high as 0.1400, 0.1395, and 0.1396,
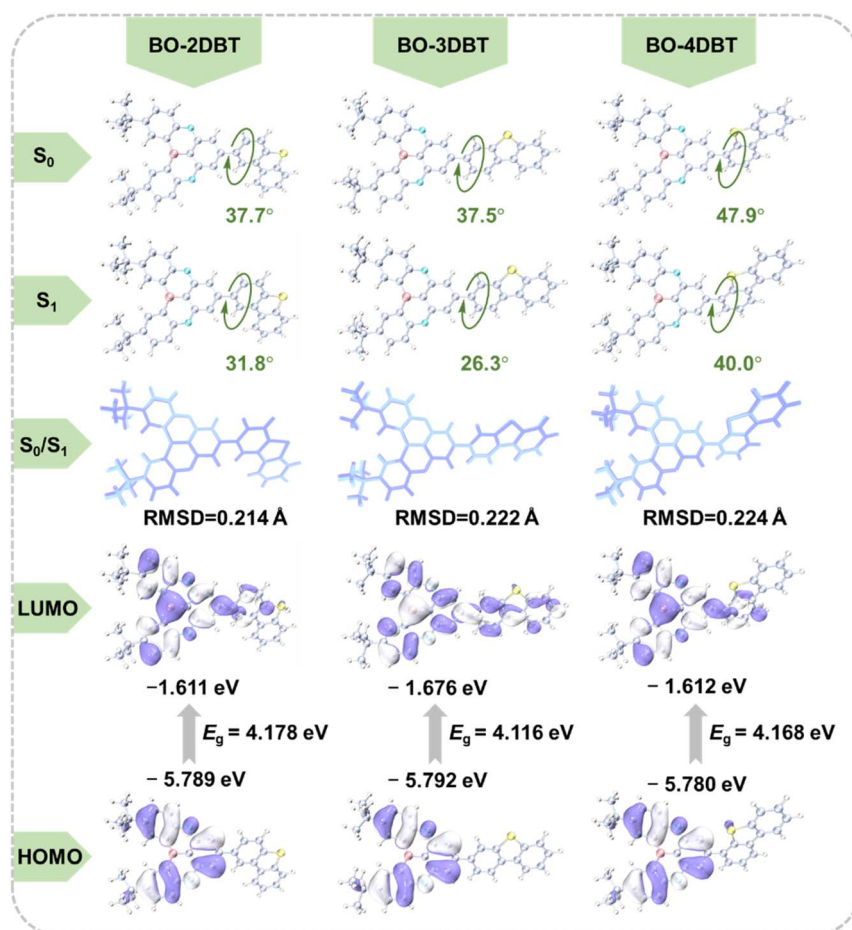

Fig. 2 Optimized S_0 and S_1 geometries, molecular relaxation in S_0/S_1 transitions and distributions of the frontier molecular orbitals of BO-2DBT, BO-3DBT, and BO-4DBT.
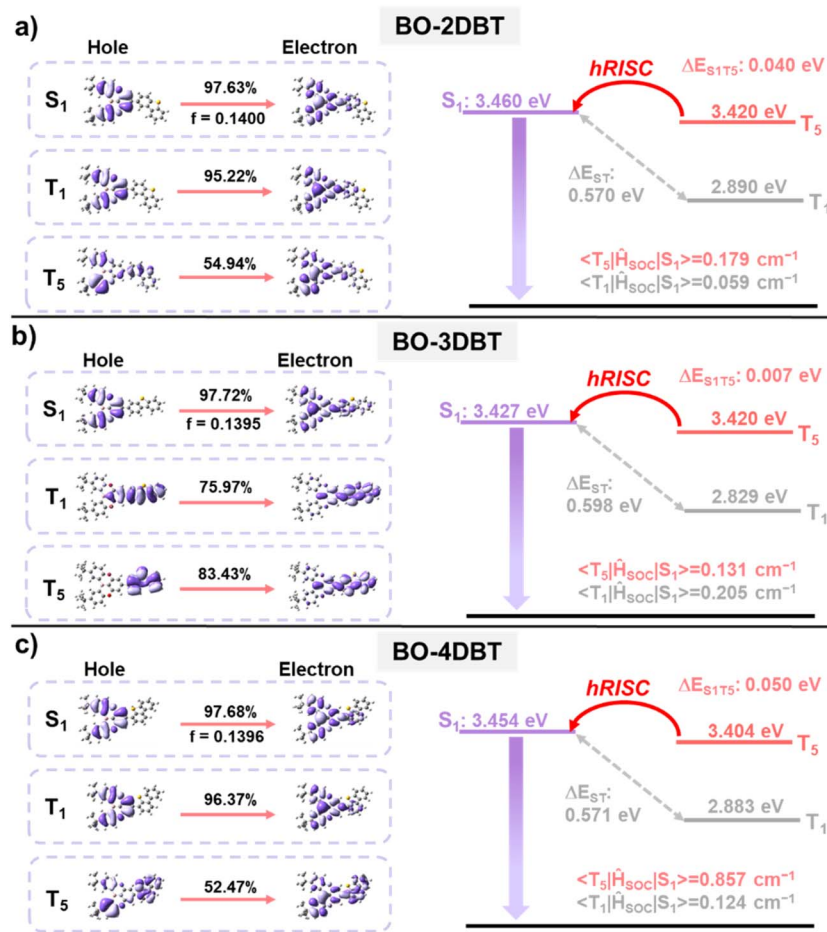
Fig. 3 NTO analysis of S_1, T_1, and T_5 excited states, and their calculated energy level diagrams with SOC values for (a) BO-2DBT, (b) BO-3DBT, and (c) BO-4DBT.

respectively, which is conducive to increasing the radiative decay rate (k_r). The lowest triplet (T_1) states of BO-2DBT and BO-4DBT show similar orbital configurations to their S_1 (Fig. 3 and Table S1), resulting in small SOC matrix elements of 0.059 and 0.124 cm^{-1}, respectively, while BO-3DBT exhibits a high SOC value of 0.205 cm^{-1} due to the different orbital configurations between S_1 and T_1 where the lone-pair electron of heavy-atom S clearly participates in the $S_1 \rightarrow T_1$ transition. The large singlet-triplet splitting energies (ΔE_{ST}) are estimated to be 0.570, 0.598, and 0.571 eV for BO-2DBT, BO-3DBT, and BO-4DBT, respectively (Table S1), making it difficult for RISC process from T_1 to S_1. Notably, compared to their S_1 state, the high-lying triplet excited state (T_5) in BO-2DBT, BO-3DBT, and BO-4DBT exhibits distinct excitation characteristics where the sulfur atoms are involved in the hole distributions. There are minimal energy differences of 0.040, 0.007, and 0.050 eV and SOC matrix elements of 0.179, 0.131, and 0.857 cm^{-1} between the S_1 and the T_5, respectively, which suggests the feasibility of a hot-exciton mechanism involving the high-lying reverse intersystem crossing (hRISC) process from T_5 to S_1, as supported by Fermi's golden rule[31,32] and El-Sayed's rule.[33] This enhances the utilization efficiency of triplet excitons in the EL process.[34–36]

Furthermore, k_{RISC} and the intersystem crossing rate (k_{ISC}) between S_1 and triplet state can be calculated using both the semiclassical Marcus theory[37,38] and Fermi's golden rule[31,32] as follows:

$$k_{RISC} = \frac{\left\langle S_1 | \hat{H}_{SOC} | T_n \right\rangle^2}{\hbar} \sqrt{\frac{\pi}{\lambda k_B T}} \exp\left[-\frac{(\Delta E_{ST} + \lambda)^2}{4\lambda k_B T} \right] \quad (1)$$

$$k_{ISC} = \frac{\left\langle S_1 | \hat{H}_{SOC} | T_n \right\rangle^2}{\hbar} \sqrt{\frac{\pi}{\lambda k_B T}} \exp\left[-\frac{(\Delta E_{ST} - \lambda)^2}{4\lambda k_B T} \right] \quad (2)$$

Here, $\hbar$ represents the reduced Planck constant. $\langle S_1 | \hat{H}_{SOC} | T_n \rangle$ signifies the SOC matrix element between S_1 and the involved triplet state. k_B denotes the Boltzmann constant, while T is the temperature which is set to 300 K constantly. λ represents the reorganization energy associated with the transition between S_1 and T_n, which is presumed to possess plausible values of either 0.10 or 0.20 eV.[34,39]

As presented in Table S2, when λ is assumed to be 0.20 eV, the $k_{RISC(T_1 \rightarrow S_1)}$ values of BO-2DBT, BO-3DBT, and BO-4DBT are notably small, calculated to be 7.11×10^{-7}, 1.03×10^{-6}, and 2.91×10^{-6} s^{-1}, respectively, due to their quite large ΔE_{ST}
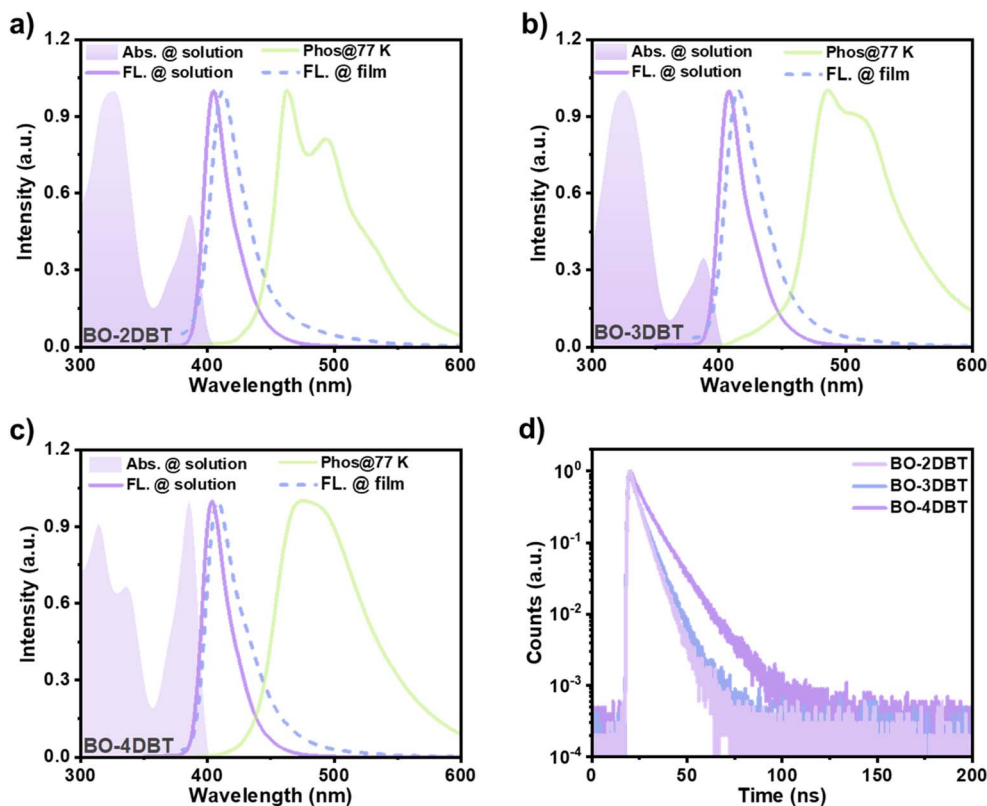
Fig. 4 UV-Vis absorption and PL spectra in toluene (10 μM) and 5 wt% doped films of (a) BO-2DBT, (b) BO-3DBT, and (c) BO-4DBT. (d) The transient PL decay curves of the 5 wt% doped films of BO-2DBT, BO-3DBT, and BO-4DBT in the mCP host at 300 K.

values. Conversely, the $k_{ISC(S_1 \rightarrow T_1)}$ values for BO-3DBT and BO-4DBT reach 1.14×10^4 s^{-1}, while BO-2DBT exhibits a substantially lower rate of 2.67×10^3 s^{-1}. These findings suggest that the ISC process from S$_1$ to T$_1$ can be effectively mitigated in the BO-2DBT emitter, thereby minimizing exciton losses in the EL process. Regarding the hRISC process from T$_5$ to S$_1$ states, the calculated $k_{RISC(T_5 \rightarrow S_1)}$ constants are substantially larger (Table S3): 3.92×10^6 or 1.14×10^6 s^{-1} for BO-2DBT, 4.62×10^6 or 1.24×10^6 s^{-1} for BO-3DBT, and 6.79×10^7 or 2.06×10^7 s^{-1} for BO-4DBT, depending on λ values of 0.10 or 0.20 eV, respectively. Notably, BO-4DBT demonstrates a $k_{RISC(T_5 \rightarrow S_1)}$ value nearly one order of magnitude higher than those of BO-2DBT and BO-3DBT, implying superior exciton utilization efficiency (EUE) in OLEDs. However, concurrently, it is observed that the $k_{ISC(S_1 \rightarrow T_5)}$ values of BO-4DBT are one to two orders of magnitude greater than those of BO-2DBT and BO-3DBT. This significant disparity in $k_{ISC(S_1 \rightarrow T_5)}$ constants may facilitate triplet exciton aggregation, consequently resulting in a diminution of device efficiency. The results demonstrate that sulfur atom proximity to the BO core enhances the heavy-atom effect,[40] leading to increased SOC values. However, this geometric perturbation also induces greater molecular distortion, which concurrently elevates k_{ISC}, and reduces PLQY in the BO-4DBT molecule.

Photophysical properties

The ultraviolet-visible (UV-Vis) absorption and steady-state photoluminescence (PL) spectra of BO-2DBT, BO-3DBT, and BO-4DBT were investigated in dilute toluene solutions (10 μM) at room temperature. As depicted in Fig. 4a–c and Table 1, the strong absorption band in the 300–360 nm region can be attributed to the π–π* transition of the acceptor unit and donor unit. The E_gs are deduced from the onset of absorption spectra to be 3.09, 3.06 and 3.10 eV for BO-2DBT, BO-3DBT, and BO-4DBT, respectively. Compared to the isolated BO unit, the slightly red-shifted absorption peaks at 386–388 nm that maintain some of the sharpness of the S$_1$ transition for the BO acceptor moiety can be assigned to the hybrid SR-CT and LR-CT transitions.[26] The fluorescence spectra exhibited ultrapure violet emission with peaks at 405, 408, and 404 nm, and small FWHMs of 23, 22, and 22 nm for BO-2DBT, BO-3DBT, and BO-4DBT, corresponding to CIE coordinates of (0.166, 0.011), (0.165, 0.013), and (0.166, 0.011), respectively.

Their spectral shapes closely resemble that of the parental BO unit, aligning with the predominantly SR-CT nature of the S$_1$ excited state. As the solvent polarity increases (Fig. S18–S20), the emission spectra of BO-2DBT, BO-3DBT, and BO-4DBT exhibit slight bathochromic shift accompanied by broadened FWHM values, whereas their absorption spectra are hardly changed in the different solvents, indicating that their S$_1$ states are mainly dominated by a SR-CT characteristic with a small portion of LR-CT characteristic in the excited state, which coincided well with the theoretically calculated result.[41] Moreover, the Stokes shifts of BO-2DBT, BO-3DBT, and BO-4DBT are estimated to be 19, 20, and 18 nm, respectively, while their PLQYs are 67%, 81%, and

Table 1 The photophysical and electrochemical properties of BO-2DBT, BO-3DBT, and BO-4DBT

Compound	$\lambda_{abs}{}^a$ [nm]	$\lambda_{em}{}^{a/b}$ [nm]	PLQY$^{a/b}$ [%]	FWHM^a [nm eV^{-1}]	FWHM^b [nm eV^{-1}]	τ^b [ns]	$k_r{}^b$ [×10^8 s^{-1}]	$k_{nr}{}^b$ [×10^8 s^{-1}]	$E_{HOMO}/E_{LUMO}/E_g{}^c$ [eV]	$E_{S_1}/E_{T_1}/\Delta E_{ST}{}^d$ [eV]
BO-2DBT	326, 386	405/412	67/59	23/0.172	32/0.229	4.74	1.24	0.87	−5.75/−2.66/3.09	3.06/2.68/0.38
BO-3DBT	324, 388	408/415	81/63	22/0.162	35/0.246	5.07	1.23	0.74	−5.78/−2.72/3.06	3.04/2.55/0.49
BO-4DBT	314, 386	404/408	38/23	22/0.166	33/0.239	8.12	0.28	0.95	−5.86/−2.76/3.10	3.07/2.60/0.47

^{a} Measured in toluene (10 μM) at 300 K. ^{b} Measured in the 5 wt% doped films at 300 K. ^{c} HOMO energy level (E_{HOMO}) obtained from CV measurement, the optical gap (E_g) deduced from the onset of absorption spectrum, and the LUMO energy level (E_{LUMO}) calculated from $E_{LUMO} = E_{HOMO} + E_g$. ^{d} S$_1$ energy level (E_{S_1}) obtained from the peaks of emission spectra in toluene (10 μM) at 300 K and T$_1$ energy level (E_{T_1}) obtained from the peaks of phosphorescence spectra in toluene (10 μM) at 77 K, $\Delta E_{ST} = E_{S_1} - E_{T_1}$.

38%, respectively, in toluene solution. Notably, their doped films with 5 wt% dispersed into 1,3-bis(carbazol-9-yl)benzene (mCP) host show slightly red-shifted and narrowband emission with peaks at 412, 415, and 408 nm, FWHMs of 32, 35, and 33 nm, as well as PLQYs of 59%, 63%, and 23%, respectively, compared with solutions, which should be attributed to the enhanced intermolecular interactions in the solid films. The low PLQY of BO-4DBT could be attributed to the non-radiative decay pathway caused by the ISC process. The energies of S$_1$ are estimated from the peak value of their PL spectra to be 3.06, 3.04, and 3.07 eV, while their T$_1$ energies are estimated to be 2.68, 2.55, and 2.60 eV, resulting in ΔE_{ST}s of 0.38, 0.49 and 0.47 eV for BO-2DBT, BO-3DBT, and BO-4DBT, respectively. The significantly large ΔE_{ST} values observed effectively rule out the involvement of the TADF mechanism. Furthermore, transient PL decay measurements were systematically conducted for all emitters in both doped films and various solutions. As illustrated in Fig. S21, S22 and 4d, these measurements reveal first-order exponential decays with nanosecond lifetimes. Notably, microsecond-scale delayed fluorescence components are absent in the doped films under microsecond-range detection windows, as confirmed from the transient PL decay profiles shown in Fig. S23a. These findings collectively preclude the possibility of TADF contributions. The doped films of BO-2DBT, BO-3DBT, and BO-4DBT exhibit fluorescence lifetimes of 4.74, 5.07, and 8.12 ns, respectively. BO-2DBT exhibits a shorter fluorescence lifetime than others, indicating faster exciton decay, which can effectively mitigate exciton quenching in the device. The k_r values of up to 1.24×10^8 and 1.23×10^8 s^{-1} are recorded for BO-2DBT and BO-3DBT, respectively, while that of BO-4DBT has fallen to 0.28×10^8 s^{-1} with a high k_{nr} of 0.95×10^8 s^{-1}. The positional variation of heavy sulfur atom exerts a minimal impact on the emission spectra of the emitters; however, the vibrational coupling and molecular conformational changes induced by sulfur incorporation profoundly modulate the radiative and non-radiative transition processes. BO-4DBT with a larger dihedral angle exhibits drastically reduced PLQY and large k_{nr} value. This could be attributed to the compromised molecular rigidity and enhanced vibrational coupling induced by the large SOC effect. Moreover, the steady-state PL spectra of BO-2DBT, BO-3DBT, and BO-4DBT in N$_2$ and air atmospheres were recorded. As shown in Fig. S23b, c and d, the emission can be partially quenched by oxygen, which indicates that triplet excitons participate in the luminescence

process. Combining theoretical analysis, the hot-exciton mechanism involving the hRISC process is the main pathway for the utilization of triplet excitons.

Single crystals

To characterize the impact of constitutional isomerism on the molecular conformation and packing structure, the single crystals of BO-2DBT and BO-4DBT were obtained through gradual solvent evaporation (from the dilute mixed solution of dichloromethane/acetone). The crystal structures of BO-2DBT and BO-4DBT were determined by single-crystal X-ray diffraction (XRD) analysis, and the corresponding crystal parameters are listed in Table S4. As depicted in Fig. S24 and S25, BO-2DBT exhibits two moderately distorted molecular conformations with the dihedral angles of 24.48° and 28.20° between the BO and DBT units, as well as 9.95° and 18.42° between the two phenyl rings within the BO skeleton. The dimers are arranged in a staggered step fashion along the molecular transverse axis, with intermolecular interactions predominantly comprising π–π stacking at distances ranging from 3.479 to 3.663 Å, and C–H⋯π interactions spanning 2.882 Å. These interactions fortify molecular rigidity, which is advantageous for mitigating molecular vibrations and structural relaxation.[42,43] Consequently, they contribute to minimizing non-radiative energy loss in aggregated states, preserving high PLQY, and narrowing the emission spectrum. BO-4DBT exhibits a more distorted molecular conformation with a dihedral angle of 39.75°, whereas the BO moiety exhibits more planar configuration with a dihedral angle of 3.58° due to the double C–H⋯O interactions (2.656 Å) with the adjacent BO skeleton. Intriguingly, weak π–π interaction with a distance of 3.753 Å is found in the crystalline packing of BO-4DBT, which can be attributed to the large steric hindrance resulting from the altered substitution position of the DBT unit. This incompact packing mode may be responsible for suppressing concentration-caused quenching effect.[44] A significantly shorter sulfur-to-boron distance in BO-4DBT (6.602 Å) compared to BO-2DBT (10.338/10.352 Å), is one of the reasons for enhanced SOC matrix element in the BO-4DBT molecule.

Device performance

Their prominent photophysical features inspired us to further investigate the potential applications of BO-2DBT, BO-3DBT,
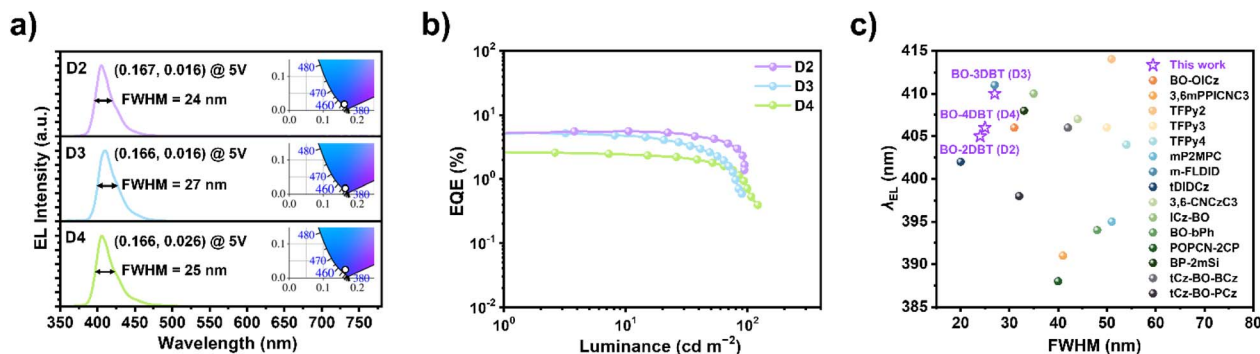
Fig. 5 (a) EL spectra of OLEDs at 5 V. Inset, corresponding CIE image. (b) EQE *versus* luminance curves. (c) EL peak wavelength *versus* FWHM of the reported representative violet OLEDs.

Table 2 The EL performance of OLEDs

Device	λ_{EL}[a] [nm]	FWHM[b] [nm eV^{-1}]	V_{on}[c] [V]	L_{max}[d] [cd m^{-2}]	CE_{max}[e] [cd A^{-1}]	PE_{max}[f] [lm W^{-1}]	EQE_{max}[g] [%]	CIE[h] (x, y)
D2	405	24/0.179	4.0	94	0.38	0.30	5.57	(0.167, 0.016)
D3	410	27/0.196	4.0	129	0.49	0.39	5.21	(0.166, 0.016)
D4	406	25/0.185	3.8	147	0.36	0.29	2.60	(0.166, 0.026)
D22	405	25/0.187	3.8	2474	0.62	0.25	7.90	(0.166, 0.014)

[a] EL peak wavelength at 5 V. [b] Full width at half maximum at 5 V. [c] Turn-on voltage at 1 cd m^{-2}. [d] Maximum luminance. [e] Maximum current efficiency. [f] Maximum power efficiency. [g] Maximum external quantum efficiency. [h] CIE coordinates at 5 V.

and BO-4DBT in OLEDs. To alleviate the exciton quenching effect, vacuum-deposited doped devices (D2, D3, and D4) with 5 wt% doping ratios in the low-polarity mCP host were fabricated with the following device architecture: ITO/HAT-CN (20 nm)/TAPC (40 nm)/TCTA (10 nm)/mCP (5 nm)/EML (20 nm)/DPEPO (5 nm)/TmPyPB (35 nm)/LiF (1 nm)/Al (100 nm). Here, devices D2, D3, and D4 correspond to the emitters BO-2DBT, BO-3DBT, and BO-4DBT, respectively; indium tin oxide (ITO) and aluminum (Al) were applied as the anode and cathode, respectively; dipyrazino[2,3-f:2′,3′-h]quinoxaline-2,3,6,7,10,11-hexacarbonitrile (HAT-CN) and lithium fluoride (LiF) acted as the hole and electron injecting layers, respectively; high-mobility 4,4′-cyclohexylidenebis[N,N-bis(4-methylphenyl)benzenamine] (TAPC) and 1,3,5-tris(3-pyridyl-3phenyl)benzene (TmPyPB) were used as the hole and electron transporting layers, respectively; mCP and bis[2(diphenylphosphino)-phenyl]ether oxide (DPEPO) were applied as the electron and hole blocking layers, respectively; 4,4′,4-tris(carbazol-9-yl)triphenylamine (TCTA) acted as the buffer layer for stepped progression of the HOMO energy levels. The molecular structures of the organic materials used in the device are provided in Fig. S26. Device structures and EL performance are shown in Fig. 5 and S27, and relevant data are summarized in Table 2.

As shown in Fig. 5, all the devices emit stable ultrapure violet light with the EL peak/FWHM values of 405/24 nm for D2, 410/27 nm for D3, and 406/25 nm for D4, corresponding to CIE coordinates of (0.167, 0.016), (0.166, 0.016), and (0.166, 0.026), respectively, which are in good agreement with their corresponding PL spectra. Notably, devices D2 and D3 with BO-2DBT and BO-3DBT, respectively, as emitters achieve impressive

EQE_{max}s of 5.57% and 5.21%, while the EQE_{max} of the BO-4DBT-based device D4 is only 2.60%, resulting from its poor PLQY. To the best of our knowledge, these values represent a breakthrough and are one of the narrowest reported for the OLEDs with an EL peak wavelength ≤415 nm (Fig. 5c). The poorest performance in BO-4DBT-based device D4 can be ascribed to its low PLQY and long fluorescence lifetime. Assuming a light outcoupling efficiency of 20–30% and a radiative exciton efficiency of 25%, the theoretical EQE_{max} values can be estimated to be 2.95–4.43%, 3.15–4.73%, and 1.15–1.73%, for BO-2DBT, BO-3DBT, and BO-4DBT, respectively, which are lower than the experimentally obtained EQE_{max} in the devices D2, D3, and D4. This implies that several triplet excitons are converted to singlets in the EL process. The good linear relationships between luminance and current density illustrate that the triplet–triplet annihilation mechanism can be excluded (Fig. S29). Combining photophysical and theoretical analysis, the hot-exciton mechanism that involves the hRISC process from T_5 to S_1 is the main reason for achieving the utilization of triplet excitons.

Given the exceptional overall performance of BO-2DBT, we further optimized its device architecture (D22) as follows: ITO/HAT-CN (20 nm)/TAPC (40 nm)/TCTA (10 nm)/mCP (5 nm)/mCP: 5 wt% BO-2DBT (20 nm)/TPBi (30 nm)/LiF (1 nm)/Al (100 nm). In this structure, 1,3,5-tri(phenyl-2-benzimidazolyl)-benzene (TPBi) functions as both the hole-blocking and electron-transporting layer. Notably, device D22 demonstrates a substantial enhancement in EL efficiency relative to device D2. As illustrated in Fig. 6, S29, and Table 2, the device achieves a low turn-on voltage of 3.8 V and a maximum luminance of
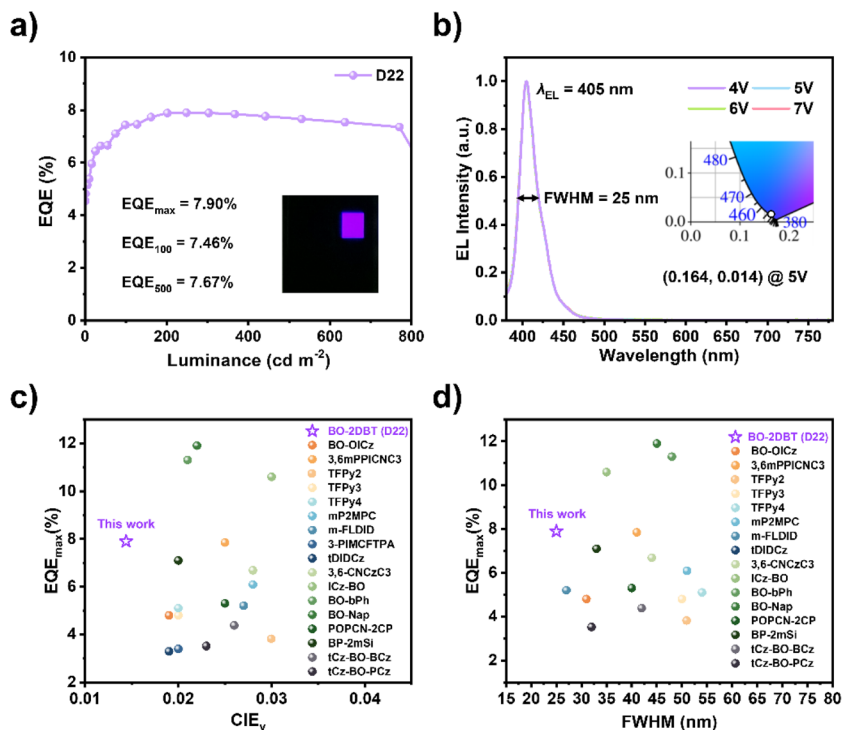
Fig. 6 (a) EQE *versus* luminance curves. Inset, corresponding light–emitting device. (b) EL spectra of OLEDs at different voltages. Inset, corresponding CIE image. (c) EQE_{max} *versus* CIE_y of the reported representative violet OLEDs ($CIE_y \leq 0.03$). (d) EQE_{max} *versus* FWHM of the reported representative violet OLEDs.

2474 cd m^{-2}. The EQE reaches a peak value of 7.90%, remaining at 7.67% under a practical luminance of 500 cd m^{-2}, indicative of minimal efficiency roll-off. Meanwhile, D22 retains stable narrowband violet emission with an EL peak at 405 nm, and a FWHM of 25 nm, corresponding to high color purity with the CIE coordinates of (0.166, 0.014). To our knowledge, device D22 represents one of the most advanced violet OLEDs fabricated utilizing oxygen-bridged boron emitters (Table S5). The CIE_y of 0.014 marks the lowest value documented to date among all reported OLEDs (Fig. 5c, d and Table S6), establishing D22 as a breakthrough in ultrapure violet OLED technology. Additionally, inspired by the good solubility of all three emitters, the simple solution-processed OLEDs were fabricated with a low doping concentration of 2 wt% in mCP. As shown in Fig. S31 and Table S7, the solution-processed device incorporating BO-2DBT achieves the highest EL performance, exhibiting a maximum EQE of 6.97%, an EL peak at 410 nm, and a FWHM of 30 nm. These results underscore the superiority of target emitters in terms of color purity.

Conclusions

In conclusion, by precisely manipulating the connection sites between the peripheral sulfur-containing DBT group and BO skeleton, we have designed and synthesized three ultrapure violet hot-exciton emitters, BO-2DBT, BO-3DBT, and BO-4DBT, exhibiting hybrid LR/SR-CT characteristics. Systematic variation in sulfur atom positioning induces distinct SOC interactions

between singlet and triplet excited states, enabling precise regulation of both the hRISC process from T_5 to S_1 and ISC process from S_1 to T_1. All the emitters exhibit emission peaks at 405, 408, and 404 nm in toluene solution, with the corresponding CIE coordinates of (0.166, 0.011), (0.165, 0.013), and (0.166, 0.011), respectively. Notably, BO-2DBT with an appropriately twisted geometry exhibits higher device performance, yielding ultrapure violet emission with CIE coordinates of (0.166, 0.014), a considerable EQE_{max} of 7.90% and minimal efficiency roll-off (7.67% at 500 cd m^{-2}). Overall, these findings not only emphasize the pivotal role of precise heavy-atom placement in engineering high-performance hot-exciton emitters and OLEDs but also offers a viable pathway toward realizing ultrapure violet OLEDs with superior efficiency and low efficiency roll-off.

Author contributions

Chen R., Li S., Huang H., and Ying S. – conceptualization, validation, investigation, visualization, methodology, OLED devices, data curation, software, writing – original draft; Chen R. and Li S. – theoretical calculation; Chen R., Li S., Huang H., and Tong X. –investigation (photophysics); Chen R., Li S., Liu Y., and Ying S. – formal analysis; Ying S., Liu Y., Ren Z., Liu L., and Yan S. – resources, project administration, supervision, funding acquisition; Ying S., Liu L., and Yan S. – writing – review & editing.

Conflicts of interest

There are no conflicts to declare.

Data availability

The data (experimental instrumentation, synthetic procedures, structural characterization data including NMR and MS spectra, theoretical calculations, thermodynamics data, crystallographic data, and device performance data) that support this article are available in the article itself and its SI. CCDC 2408106 (BO-2DBT) and 2408107 (BO-4DBT).[45,46] For SI and crystallographic data in CIF or other electronic format see DOI: https://doi.org/10.1039/d5sc03546e.

Acknowledgements

Notes and references

1 J. Chen, H. Liu, J. Guo, J. Wang, N. Qiu, S. Xiao, J. Chi, D. Yang, D. Ma and Z. Zhao, *Angew. Chem., Int. Ed.*, 2022, **61**, e202116810.

2 S. Chen and H. Xu, *Chem. Soc. Rev.*, 2021, **50**, 8639–8668.

3 Z. Yang, Z. Mao, Z. Xie, Y. Zhang, S. Liu, J. Zhao, J. Xu, Z. Chi and M. P. Aldred, *Chem. Soc. Rev.*, 2017, **46**, 915–1016.

4 H. Zhang, G. Li, X. Guo, K. Zhang, B. Zhang, X. Guo, Y. Li, J. Fan, Z. Wang and D. Ma, *Angew. Chem., Int. Ed.*, 2021, **133**, 22415–22421.

5 K. Zhang, Z. Zhou, D. Liu, Y. Chen, S. Zhang, J. Pan, X. Qiao, D. Ma, S.-J. Su and W. Zhu, *Angew. Chem., Int. Ed.*, 2024, **63**, e202407502.

6 H. L. Lee, W. J. Chung and J. Y. Lee, *Small*, 2020, **16**, 1907569.

7 S. Zou, X. Chen, S. Yang, S. Kumar, Y. Qu, Y. Yu, M. K. Fung, Z. Jiang and L. Liao, *Adv. Opt. Mater.*, 2020, **8**, 2001074.

8 J. M. Ha, S. H. Hur, A. Pathak, J. E. Jeong and H. Y. Woo, *NPG Asia Mater.*, 2021, **13**, 53.

9 Y. Huo, H. Qi, S. He, J. Li, S. Song, J. Lv, Y. Liu, L. Peng, S. Ying and S. Yan, *Aggregate*, 2023, **4**, e391.

10 G. Li, K. Xu, J. Zheng, X. Fang, W. Lou, F. Zhan, C. Deng, Y.-F. Yang, Q. Zhang and Y. She, *J. Am. Chem. Soc.*, 2024, **146**, 1667–1680.

11 J. Dong, L. Chen, Q. Feng and D. T. Yang, *Angew. Chem., Int. Ed.*, 2025, **64**, e202417200.

12 L. Ge, W. Zhang, Y.-H. Hao, M. Li, Y. Liu, M. Zhou and L.-S. Cui, *J. Am. Chem. Soc.*, 2024, **146**, 32826–32836.

13 K. Jiang, X. Chang, J. Zhu, T. Zhu, J. Yu, Y. Wang, Y. Zhang, D. Ma and W. Zhu, *Angew. Chem., Int. Ed.*, 2025, **64**, e202421520.

14 T. Hatakeyama, K. Shiren, K. Nakajima, S. Nomura, S. Nakatsuka, K. Kinoshita, J. Ni, Y. Ono and T. Ikuta, *Adv. Mater.*, 2016, **28**, 2777–2781.

15 T. Yang, N. Qiu, X. Lan, X. Dong, B. Z. Tang and Z. Zhao, *J. Phys. Chem. C*, 2024, **128**, 16085–16092.

16 J. Park, J. Moon, U. Jo, S. Han, D. R. Lee, H. J. Ahn, J. Y. Kim, J. H. Baek and J. Y. Lee, *Adv. Opt. Mater.*, 2024, **12**, 2302791.

17 X. Q. Gan, Z. M. Ding, D. H. Liu, W. Q. Zheng, B. Ma, H. Zhang, X. Chang, L. Wang, Y. Liu and X. Wu, *Adv. Opt. Mater.*, 2023, **11**, 2300195.

18 N. Aizawa, Y. Harabuchi, S. Maeda and Y.-J. Pu, *Nat. Commun.*, 2020, **11**, 3909.

19 R. A. Marcus, *Angew. Chem., Int. Ed.*, 1993, **32**, 1111–1121.

20 Y. X. Hu, J. Miao, T. Hua, Z. Huang, Y. Qi, Y. Zou, Y. Qiu, H. Xia, H. Liu and X. Cao, *Nat. Photonics*, 2022, **16**, 803–810.

21 Y. Zou, M. Yu, Y. Xu, Z. Xiao, X. Song, Y. Hu, Z. Xu, C. Zhong, J. He and X. Cao, *Chem*, 2024, **10**, 1485–1501.

22 H. Hirai, K. Nakajima, S. Nakatsuka, K. Shiren, J. Ni, S. Nomura, T. Ikuta and T. Hatakeyama, *Angew. Chem., Int. Ed.*, 2015, **127**, 13785–13789.

23 Y. Lee and J. I. Hong, *Adv. Opt. Mater.*, 2021, **9**, 2100406.

24 Y. Xie, L. Hua, Z. Wang, Y. Liu, S. Ying, Y. Liu, Z. Ren and S. Yan, *Sci. China Chem.*, 2023, **66**, 826–836.

25 T. Lu and F. Chen, *J. Comput. Chem.*, 2012, **33**, 580–592.

26 R. Z. An, Y. Sun, H. Y. Chen, Y. Liu, A. Privitera, W. K. Myers, T. K. Ronson, A. J. Gillett, N. C. Greenham and L. S. Cui, *Adv. Mater.*, 2024, **36**, 2313602.

27 T. Chen, J. Lou, H. Wu, J. Luo, D. Yang, X. Qiao, H. Zhang, B. Z. Tang and Z. Wang, *Adv. Opt. Mater.*, 2023, **11**, 2301053.

28 H. Qi, D. Xie, Z. Gao, S. Wang, L. Peng, Y. Liu, S. Ying, D. Ma and S. Yan, *Chem. Sci.*, 2024, **15**, 11053–11064.

29 J. Jin, M. Chen, H. Jiang, B. Zhang, Z. Xie and W.-Y. Wong, *ACS Mater. Lett.*, 2024, **6**, 3246–3253.

30 Y. Dai, J. Xu, X. Lei, Q. Y. Meng and J. Qiao, *Adv. Funct. Mater.*, 2025, **35**, 2412780.

31 V. Lawetz, G. Orlandi and W. Siebrand, *J. Chem. Phys.*, 1972, **56**, 4058–4072.

32 G. W. Robinson and R. Frosch, *J. Chem. Phys.*, 1963, **38**, 1187–1203.

33 M. El-Sayed, *J. Chem. Phys.*, 1963, **38**, 2834–2838.

34 P. K. Samanta, D. Kim, V. Coropceanu and J.-L. Brédas, *J. Am. Chem. Soc.*, 2017, **139**, 4042–4051.

35 I. S. Park, K. Matsuo, N. Aizawa and T. Yasuda, *Adv. Funct. Mater.*, 2018, **28**, 1802031.

36 Y. Xu, C. Li, Z. Li, Q. Wang, X. Cai, J. Wei and Y. Wang, *Angew. Chem., Int. Ed.*, 2020, **59**, 17442–17446.

37 R. A. Marcus, *J. Chem. Phys.*, 1956, **24**, 966–978.

38 R. Marcus, *J. Chem. Phys.*, 1984, **81**, 4494–4500.

39 Y. Luo, S. Li, Y. Zhao, C. Li, Z. Pang, Y. Huang, M. Yang, L. Zhou, X. Zheng and X. Pu, *Adv. Mater.*, 2020, **32**, 2001248.

40 Y. Zou, M. Yu, Y. Xu, Z. Xiao, X. Song, Y. Hu, Z. Xu, C. Zhong, J. He, X. Cao, K. Li, J. Miao and C. Yang, *Chem*, 2024, **10**, 1485–1501.

41 F. Huang, X. C. Fan, Y. C. Cheng, Y. Xie, S. Luo, T. Zhang, H. Wu, X. Xiong, J. Yu and D. D. Zhang, *Adv. Opt. Mater.*, 2023, **11**, 2202950.

42 Y. Zhang, J. Wei, D. Zhang, C. Yin, G. Li, Z. Liu, X. Jia, J. Qiao and L. Duan, *Angew. Chem., Int. Ed.*, 2022, **61**, e20211320 6.

43 Y. Liu, X. Xiao, Z. Huang, D. Yang, D. Ma, J. Liu, B. Lei, Z. Bin and J. You, *Angew. Chem., Int. Ed.*, 2022, **61**, e202210210.

44 G. Li, J. Pu, Z. Yang, H. Deng, Y. Liu, Z. Mao, J. Zhao, S. J. Su and Z. Chi, *Aggregate*, 2023, **4**, e382.

45 R. Chen, S. Li, H. Huang, X. Tong, Y. Liu, Z. Ren, S. Ying, L. Liu and S. Yan, CCDC 2408106: Experimental Crystal Structure Determination, 2024, DOI: **10.5517/ccdc.csd.cc2lttv3**.

46 R. Chen, S. Li, H. Huang, X. Tong, Y. Liu, Z. Ren, S. Ying, L. Liu and S. Yan, CCDC 2408107: Experimental Crystal Structure Determination, 2024, DOI: **10.5517/ccdc.csd.cc2lttw4**.